Stem Cell Reports
Article

OPEN ACCESS

Neural Stem Cells of Parkinson's Disease Patients Exhibit Aberrant Mitochondrial Morphology and Functionality

Jonas Walter,[1,7] Silvia Bolognin,[1,7] Paul M.A. Antony,[1,8] Sarah L. Nickels,[1,2,8] Suresh K. Poovathingal,[1,8,9] Luis Salamanca,[1] Stefano Magni,[1] Rita Perfeito,[3] Fredrik Hoel,[4] Xiaobing Qing,[1] Javier Jarazo,[1] Jonathan Arias-Fuenzalida,[1] Tomasz Ignac,[1] Anna S. Monzel,[1] Laura Gonzalez-Cano,[1] Luis Pereira de Almeida,[3,5] Alexander Skupin,[1,6] Karl J. Tronstad,[4] and Jens C. Schwamborn[1,*]

[1]Luxembourg Centre for Systems Biomedicine (LCSB), University of Luxembourg, 4362 Belvaux, Luxembourg
[2]Life Science Research Unit (LSRU), University of Luxembourg, 4362 Belvaux, Luxembourg
[3]CNC-Center for Neuroscience and Cell Biology, University of Coimbra, Rua Larga, Coimbra 3004-504, Portugal
[4]Department of Biomedicine, University of Bergen, 5020 Bergen, Norway
[5]Faculty of Pharmacy, University of Coimbra, Coimbra 3000-548, Portugal
[6]Center for Research of Biological Systems, University of California San Diego, La Jolla, CA 92093, USA
[7]Co-first authors
[8]These authors contributed equally
[9]Present address: Single Cell Analytics & Microfluidics Core, VIB-KU Leuven, Herestraat 49, 3000 Leuven, Belgium
*Correspondence: jens.schwamborn@uni.lu
https://doi.org/10.1016/j.stemcr.2019.03.004

SUMMARY

Emerging evidence suggests that Parkinson's disease (PD), besides being an age-associated disorder, might also have a neurodevelopment component. Disruption of mitochondrial homeostasis has been highlighted as a crucial cofactor in its etiology. Here, we show that PD patient-specific human neuroepithelial stem cells (NESCs), carrying the LRRK2-G2019S mutation, recapitulate key mitochondrial defects previously described only in differentiated dopaminergic neurons. By combining high-content imaging approaches, 3D image analysis, and functional mitochondrial readouts we show that LRRK2-G2019S mutation causes aberrations in mitochondrial morphology and functionality compared with isogenic controls. LRRK2-G2019S NESCs display an increased number of mitochondria compared with isogenic control lines. However, these mitochondria are more fragmented and exhibit decreased membrane potential. Functional alterations in LRRK2-G2019S cultures are also accompanied by a reduced mitophagic clearance via lysosomes. These findings support the hypothesis that preceding mitochondrial developmental defects contribute to the manifestation of the PD pathology later in life.

INTRODUCTION

Parkinson's disease (PD) is a neurodegenerative disorder affecting 1% of the population more than 60 years old (Tysnes and Storstein, 2017). The key histopathological hallmark of the disease is the degeneration of dopaminergic neurons in the substantia nigra of the midbrain. The cause of the disease is still unknown. However, a complex interplay between genetic and environmental factors might contribute to its pathogenesis (for review see Burbulla and Kruger, 2011). The dysregulation of mitochondrial function has been highlighted as a crucial player, because complex I activity was shown to be reduced in PD patients (Schapira et al., 1990). More recently, various PD-specific cellular models revealed impaired mitochondrial morphology and transport, increased release of reactive oxygen species (ROS), and reduced mitochondrial motility compared with controls (Hsieh et al., 2016; Smith et al., 2016; Trimmer et al., 2000). Dopaminergic neurons in the substantia nigra have higher energy demands compared with other types of neurons because of the production of the neurotransmitter dopamine, and the particularly long, highly branched, and unmyelinated axons (Pissadaki and Bolam, 2013). Therefore, they are particularly susceptible to mitochondrial dysfunctions compared with other types of neurons (for review see Haddad and Nakamura, 2015). These mitochondrial dysfunctions might be caused by genetic alterations and/or environmental impacts. Several genetic variants are associated with the risk of developing PD (Klein and Westenberger, 2012). Interestingly, mutations in the gene encoding leucine-rich repeat serine/threonine-protein kinase 2 (*LRRK2*) have been associated with both familial and sporadic PD (Funayama et al., 2002; Lesage et al., 2007; Ozelius et al., 2006). The autosomal-dominant genomic mutation (c.6055 G>A), which results in a LRRK2-p.G2019S (G2019S) substitution, is the most prevalent genetic risk factor for PD (Funayama et al., 2002; Paisan-Ruiz et al., 2004). LRRK2 cellular functions have not yet been fully defined. However, LRRK2 is thought to contribute to autophagy and mitochondrial regulation (Roosen and Cookson, 2016), microtubule dynamics (Krumova et al., 2015), microRNA activity regulation (Gonzalez-Cano et al., 2018), and vesicular trafficking (Cookson, 2016). It is located in the cytoplasm and associated with membranes (Vitte et al., 2010; West et al., 2005). Recently, LRRK2-G2019S has proven to be associated with autophagosomal-endosomal-lysosomal pathways related to mitochondrial health and biogenesis (Roosen and Cookson, 2016; Wallings et al., 2015).

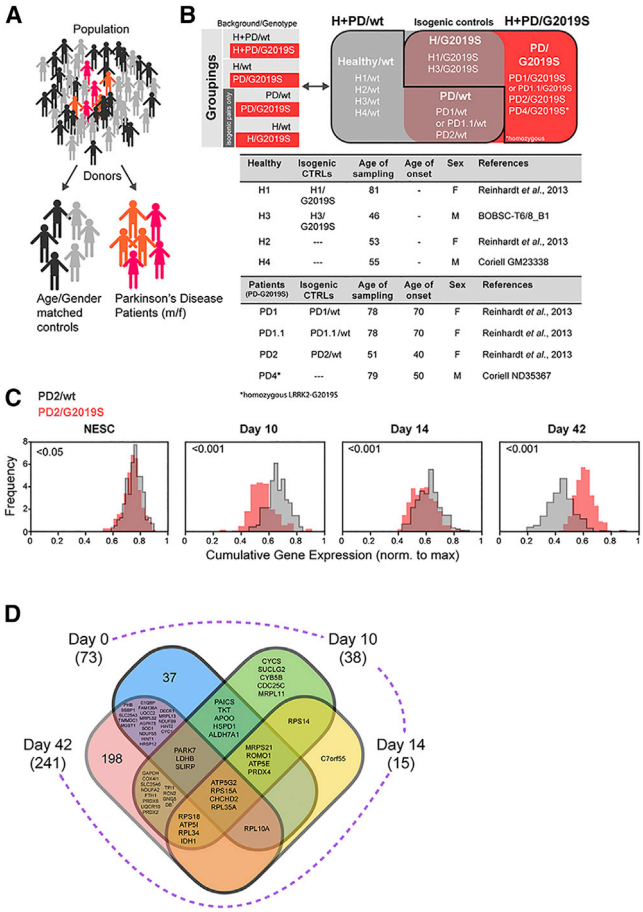

Figure 1. LRRK2-G2019S Alters Mitochondrial Gene Expression Profile

(A and B) Cartoon and tables illustrating the cell lines used and the grouping applied.

(C) Histograms showing cumulative gene expression distributions for mitochondrial-specific genes in NESCs and during dopaminergic differentiation (10, 14, and 42 days). For each cell, a score called cumulative gene expression was defined as the sum of the gene expression for all the genes associated to mitochondria (details are provided in the Experimental Procedures). These are the genes present in the targeted list of genes specific for mitochondria (Table S1), generated based on the available literature (Calvo et al., 2016). Cells having a higher cumulative gene expression are cells for which the expression of mitochondrial-specific genes is high. For each condition (PD2/WT, PD2/G2019S N = 1, n = 3) and for each day, 250 cells were considered, for a total of 2,000 cells. The statistical significance of the difference in population average between the two genotypes is indicated in each panel and was obtained by means of a z test including Bonferroni correction for multiple hypothesis testing. The frequency reported on the vertical axes represents the number of cells in each bin of the histogram, normalized in a way that each distribution has a surface equal to 1. N indicates the number of experimental repetitions, n indicates the number of technical replicates per cell line.

(D) Venn diagram representing the differentially expressed genes (DEGs) specific for mitochondria. Each ensemble contains the DEGs at a given time point. The total number of mitochondrial DEGs for the corresponding time point is indicated in brackets. The numbers indicate how many DEGs fall into the area of the Venn diagram. Where graphically possible, we report the names of the genes, instead of their number. The names of the genes common to all four time points are reported in bold in the center of the diagram. By definition, the sum of the numbers of genes appearing into each of the four ensembles is equal to the total number of DEGs for that day, reported in brackets.

Neural progenitor stem cells have been highlighted as a meaningful model for mitochondria-related disease phenotyping (Lorenz et al., 2017). Here, we use PD patient-specific induced pluripotent stem cell (iPSC)-derived neuroepithelial stem cells (NESCs) to assess mitochondrial features. NESCs are an easily accessible and highly homogeneous model representing early brain development. We observed that mitochondria in NESCs carrying the LRRK2-G2019S mutation were more fragmented and more prone to release ROS compared with isogenic controls. Also, the functionality of mitochondria was impaired in patient-specific stem cells as shown by the decreased membrane potential and respiratory capacity.

RESULTS

In our study, we used 13 human iPSC-derived NESC lines obtained from three patients carrying the LRRK2-G2019S mutation and four age- and gender-matched healthy individuals. Four isogenic NESC lines (two in which the mutation was introduced and two in which the mutation was corrected) were also generated (Figures 1A and 1B). For patient 1 two different clones were used (PD.1 and PD1.1). The use of isogenic controls enabled us to distinguish between LRRK2-G2019S-dependent and -independent phenotypes. The derivation and characterization of NESCs from iPSCs have been described previously (Reinhardt et al., 2013).

Throughout the article, unless otherwise stated, we indicate whether the donor was healthy (H) or affected by the pathology (PD). LRRK2 genotype is annotated according to the absence (WT) or presence of the LRRK2-G2019S mutation (G2019S). Cells from a healthy individual are indicated as H/WT, and after the introduction of LRRK2-G2019S as H/G2019S (isogenic control). Cells from a PD patient with the LRRK2-G2019S mutation are annotated as PD/G2019S, and after genetic correction of LRRK2-G2019S as PD/WT. The use of these groupings allowed us to distinguish between effects due to LRRK2-G2019S mutation and effects that depend on the individual's genetic background. We first compared all NESC lines only

according to their LRRK2 genotype (H + PD/G2019S versus H + PD/WT). Then, we compared cells from LRRK2-G2019S patients with cells from age- and gender-matched controls (PD/G2019S versus H/WT); third, we compared samples from PD patients with their isogenic controls (PD/G2019S versus PD/WT). Finally, we investigated the impact of introducing the LRRK2-G2019S mutation in a healthy genetic background (H/WT versus H/G2019S).

LRRK2-G2019S Induces Mitochondrial Gene Expression Alterations

Mitochondrial dysfunctions have been previously associated to LRRK2-G2019S in iPSC-derived neurons (Burbulla and Kruger, 2011). To determine whether LRRK2-G2019S mutation affected mitochondrial-related genes also at the NESC level or only after dopaminergic differentiation, we performed droplet-based (Drop-seq) single-cell RNA sequencing (RNA-seq). Here, we focused on the cells from an early-onset patient (PD2/G2019S) and the corresponding isogenic control cells (PD2/WT). We first generated a targeted list specific for mitochondrial genes (Table S1) based on an inventory of human genes encoding mitochondrial-localized proteins (www.broadinstitute.org/pubs/MitoCarta) (Calvo et al., 2016). We profiled 2,000 quality-controlled cells and, after *in silico* pre-processing of the data, we calculated cumulative gene expression scores for the mitochondrial-based defined gene list (details are provided in the Experimental Procedures section). The analysis of the cumulative gene expression distribution (Figure 1C) showed significant gene expression differences between the genotypes at the different neuronal differentiation time points assessed (10, 14, and 42 days). Interestingly, a significant difference in mitochondria-related genes was already observed in the NESCs carrying the LRRK2-G2019S compared with the LRRK2-WT, before induction of differentiation. Hence, we decided to focus our analysis on NESCs to better characterize the mitochondrial defects appearing already in this cell type. To gain more insights into the dynamics of the mitochondrial gene expression levels, for each day we computed the differentially expressed genes (DEGs) between LRRK2-WT and LRRK2-G2019S. We observed that, among the total genes (approximately 17,000) in common between all the time points in our dataset, the numbers of DEGs at days 0, 10, 14, and 42 were, respectively, 619, 531, 318, and 1,637 (Table S2). This corresponds to approximately 4%, 3%, 2%, and 10% of the total genes. Since our focus is mitochondria, we considered the DEGs that were present in Table S1. Among these mitochondria-related genes, the number, of those differentially expressed at days 0, 10, 14, and 42 were, respectively 73, 38, 15, and 241. These are equivalent to respectively 6%, 3%, 1%, and 21% of the total number of mitochondrial genes in our list. The change of this percentage across the different days reflects the trend observed in the overall percentage of DEGs across the whole genome, thus overall it is not only a feature of the mitochondria-related genes. On the other hand, the most remarkable difference is in the percentage of DEGs at day 42, which is 10% across the whole genome, but 21% (i.e., more than twice) across the list of mitochondrial genes. This indicates that the expression of mitochondria-related genes is dramatically different between LRRK2-WT and LRRK2-G2019S at day 42. We further investigated whether the genes that are differentially expressed between LRRK2-WT and LRRK2-G2019S are different or similar at different time points. We then considered the list of DEGs among the mitochondria-specific genes at each day, and intersect every possible combination of lists, and count the number of DEGs in the intersection (Figure 1D). The majority of the mitochondria-related genes are differentially expressed only at one time point. However, four genes are differentially expressed at every time point: ATP5G2, RPS15A, CHCHD2, and RPL35A. An additional 12 genes are differentially expressed at 3 different time points. Notably, PARK7 (or DJ1) is differentially expressed between LRRK2-WT and LRRK2-G2019S at days 0, 10, and 42. Interestingly, of the 16 genes that are DEGs at 3 or 4 time points, there are 3 that encode components of ATP synthases (ATP5G2, ATP5I, and ATP5E). Perhaps less surprisingly, among these 16 DEGs at 3 or 4 days, there are 5 genes that correspond to ribosomal proteins, namely RPS15A, RPS18, RPL10A, RPL34, and RPL35A, and a sixth one, RPS14, is a DEG at day 10 and 14. We also notice that, among the DEGs that are common between days 10 and 42, we find GAPDH, which codes for an enzyme that catalyzes the sixth step of glycolysis, and has been found to be implicated in several neurodegenerative diseases including PD.

LRRK2-G2019S Induces Mitochondrial Fragmentation in NESCs

Under normal physiological conditions, cells maintain a well-balanced mitochondrial fission/fusion ratio, and any divergence from this stable homeostasis indicates problems in mitochondria functionality (Youle and van der Bliek, 2012). These alterations are usually indicated by fragmented or elongated mitochondrial morphology (Wu et al., 2011). We analyzed mitochondrial morphometrics via immunocytochemistry using an antibody against the translocase of outer mitochondrial membrane 20 protein (TOM20) (Narendra et al., 2008) and established an automated high-content screening (HCS) 2D imaging single-cell analysis approach to unbiasedly quantify mitochondrial features. We analyzed the mitochondrial staining with respect to the number of mitochondria per cell (Figures 2A and S1A). NESCs carrying LRRK2-G2019S from PD patients exhibited significantly more mitochondria per

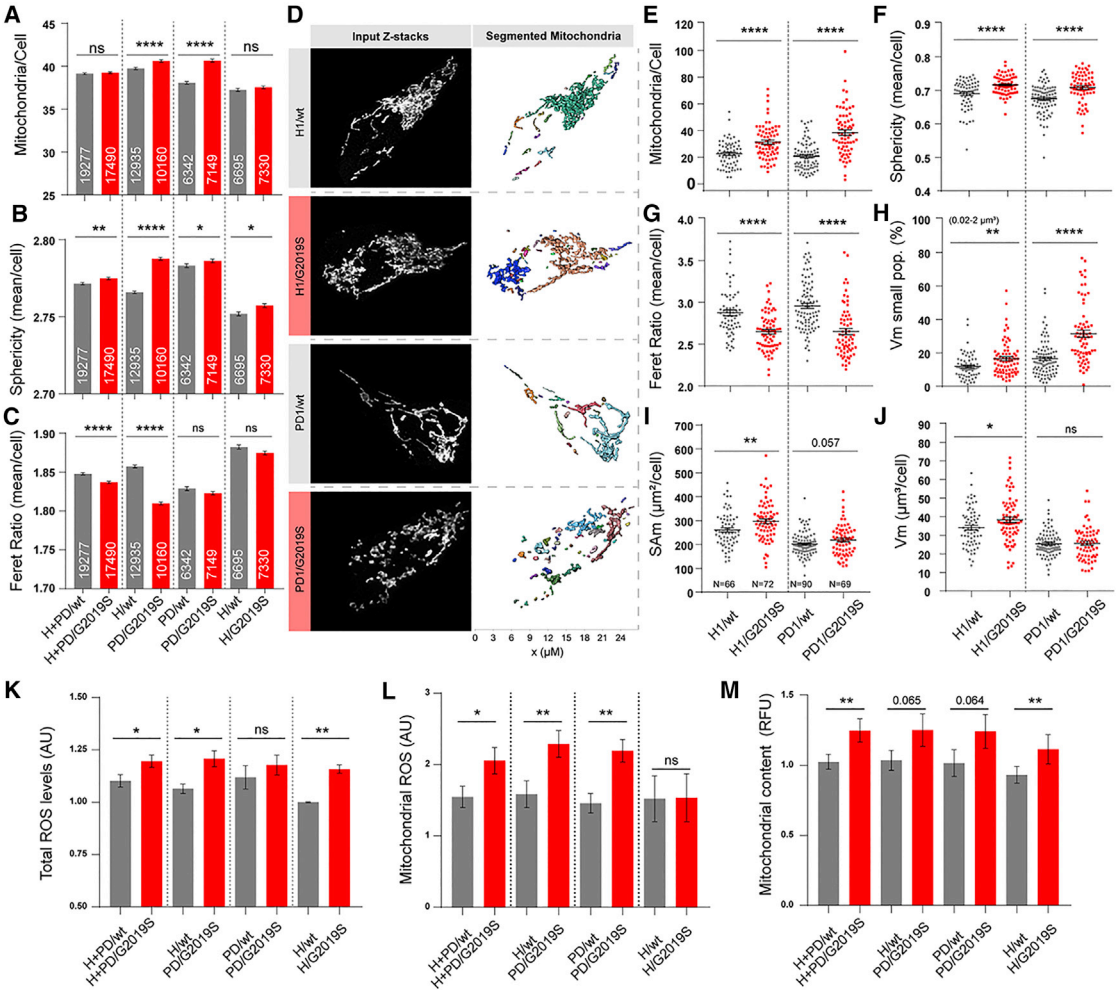

Figure 2. LRRK2-G2019S Induces Mitochondrial Fragmentation in NESCs

(A–C) Automated single-cell analysis of mitochondrial morphology in pooled groups. The number of cells is indicated in each bar (N = 3, n = 3). The following parameters were assessed: (A) number of mitochondria per cell; (B) mean mitochondrial sphericity; (C) Feret ratio.

(D–J) Unbiased/blinded manual 3D single-cell analysis of the mitochondrial features of selected cell lines (H1/WT, H1/G2019S, PD1/WT, and PD1/G2019S). Each dot plotted represents data from a single analyzed cell (n cells per group indicated in I; N = 3, n = 3). Statistical significance was determined using Student's t test. (D) Representative z stack maximum intensity projections of single cells and corresponding post-processing showing segmented mitochondria in different colors. The x-axis indicates the size of the mitochondria in μm. The following parameters were assessed: (E) number of mitochondria per cell; (F) mean mitochondrial sphericity; (G) mean Feret ratio of mitochondria; (H) surface area of mitochondria (SAm) (μm^2); (I) mitochondrial volume (Vm) per cell (μm^3); (J) percentage of small-volume mitochondria (0.02–2 μm^2).

(K) Total ROS levels normalized to H1, N = 5–6, n = 3, Mann-Whitney test was performed within isogenic groups.

(L) Mitochondrial ROS levels normalized to H1, N = 4, n = 1 Mann-Whitney test was performed within isogenic groups.

(M) Mitochondrial content measurements normalized to H1, N = 4, n = 2, Mann-Whitney test was performed within isogenic groups. For all panels, the data are presented as the mean (only 1 median) ± SEM. N indicates the number of experimental repetitions, n indicates the number of technical replicates per cell line.

cell than their isogenic controls and H individuals. Insertion of the mutation in the H background did not exert the same effect. Next, we quantified sphericity and elongation of individual mitochondria (Nikolaisen et al., 2014) and compared the mean values of these parameters per cell (Figures 2B and S1B). In agreement with the previous finding, the analysis revealed significantly higher mitochondrial sphericity in LRRK2-G2019S cultures compared with controls. We next used the Feret ratio (Igathinathane et al., 2008), which takes into account the shortest and longest extensions of mitochondria as a measure of their elongation (Figures 2C and S1C). Feret ratio analysis

showed significantly smaller ratios of Feret maxima and minima in cells from patients compared with H, indicating that these cells contained less elongated mitochondria than cells from healthy individuals. Correction of the mutation in PD patients and insertion of the mutation in H did not significantly affect this parameter.

To verify these findings and explore additional morphological details, we next conducted a detailed 3D analysis of mitochondrial morphology in NESCs. We selected two isogenic pairs derived from a healthy line (H1) and a LRRK2-G2019S carrier PD patient (PD1.1) (Figure 2D). The 3D analysis revealed an increased number of mitochondria (Figure 2E) in LRRK2-G2019S NESCs. When calculated per cell, and under mitochondrial subpopulation analyses, mitochondria from LRRK2-G2019S NESCs displayed greater sphericity (Figures 2F, S1D, and S1E), a reduced Feret ratio (Figures 2G, S1F, and S1G), and an increased volume fraction (percentage) of small mitochondria (Figure 2H) compared with isogenic controls. The total mitochondrial surface area (Figure 2I) and volume (Figures 2J, S1H, and S1I) increased in LRRK2-G2019S NESCs compared with the LRRK2-WT NESCs, suggesting that LRRK2-G2019S NESCs had an increased mitochondrial biomass. The increase did not reach statistical significance in PD patient cells when compared with their isogenic controls. Based on the results of the two different mitochondrial morphology analyses, we concluded that increased levels of mitochondrial fragmentation were present in LRRK2-G2019S NESCs. This suggests that the LRRK2-G2019S mutation interferes with mitochondrial dynamics, suggesting reduced mitochondrial quality.

LRRK2-G2019S Causes Increased Total and Mitochondrial ROS Levels

As LRRK2-G2019S induced aberrant mitochondrial morphologies, we evaluated the possible negative effects in terms of oxidative stress. Mitochondria passively release the main fraction of total cellular ROS (Turrens, 2003), and increased ROS release is a direct indicator of mitochondrial dysfunction (Lambeth et al., 2007). Therefore, we performed a general analysis of total ROS levels using a luminescence-based system. We detected significantly increased ROS levels in LRRK2-G2019S NESCs compared with controls (Figures 2K and S1J). Correction of the LRRK2-G2019S mutation in the patient lines was insufficient to significantly rescue the total ROS levels. On the other hand, the insertion of the LRRK2-G2019S mutation in the healthy background induced increased ROS levels compared with the isogenic controls. We then assessed mitochondria-specific superoxide levels using a MitoSOX probe using flow cytometry (Figures 2L, S1K, and S1L). The resulting data revealed significantly elevated mitochondrial ROS (mROS) levels in cells expressing LRRK2-G2019S. Correction of the LRRK2-G2019S mutation rescued mROS levels, but healthy control cells with the inserted mutation showed no elevation in mROS (Figure 2L). We next measured the mitochondrial content of NESCs using flow cytometry with the MitoTracker probe and observed an increased amount in NESCs carrying the LRRK2-G2019S mutation (Figures 2M, S1M, and S1N). This increase did not reach statistical significance in the comparisons H versus P and P/WT versus P/G2019S.

Overall, these results indicate that LRRK2-G2019S-expressing NESCs exhibited a higher degree of mitochondrial fragmentation and morphological alterations than mitochondria in LRRK2-WT NESCs. When comparing H/WT with H/G2019S, it was apparent that the amplitude of the phenotypes was smaller than when comparing H/WT with P/G2019S. This suggests that LRRK2-G2019S mutation plays a deleterious effect on mitochondria, which can be exacerbated by a permissive genetic background.

LRRK2-G2019S Alters Mitochondrial Functionality

To address whether LRRK2-G2019S also functionally altered mitochondria, we analyzed mitochondrial respiration and mitochondrial membrane potential (MMP). The oxygen consumption rate (OCR) was measured with the Seahorse Extracellular Flux Analyzer (Figures 3A–3D and S2A–S2E). LRRK2-G2019S NESCs showed a significantly decreased basal respiration compared with LRRK2-WT (Figures 3A and S2A). We injected oligomycin to determine the proportion of ATP-linked OCR, followed by FCCP, an uncoupling compound, used to induce maximal respiration. LRRK2-G2019S NESCs showed a significantly reduced maximal respiration capacity compared with LRRK2-WT. The same differences were observed when comparing H/WT and PD/G2019S (Figures 3B and S2B), PD/WT and PD/G2019S patients (Figures 3C and S2C), and H/WT and H/G2019S lines (Figures 3D and S2D). Proton leakage was unchanged between the tested conditions. We next analyzed MMP, another parameter indicating mitochondrial quality (Brand and Nicholls, 2011). Using TMRM dye, we detected significantly lower MMP in LRRK2-G2019S-expressing NESCs compared with LRRK2-WT (Figures 3E and S2F).

We also assessed the viability of the NESCs using propidium iodide (Pi) staining via flow cytometry. The Pi^+ quantification revealed increased cell death in LRRK2-G2019S NESC cultures compared with LRRK2-WT (Figures 3F–H). In a previous study, increased cell death was observed in NSC LRRK2-G2019S cultures after the addition of a proteasome inhibitor (Liu et al., 2012). It was previously reported that neural stem cells are competent to differentiate into neurons, astrocytes, and oligodendrocytes (Conti et al., 2005), but they do not efficiently differentiate in midbrain dopaminergic neurons (Reinhardt et al., 2013). This

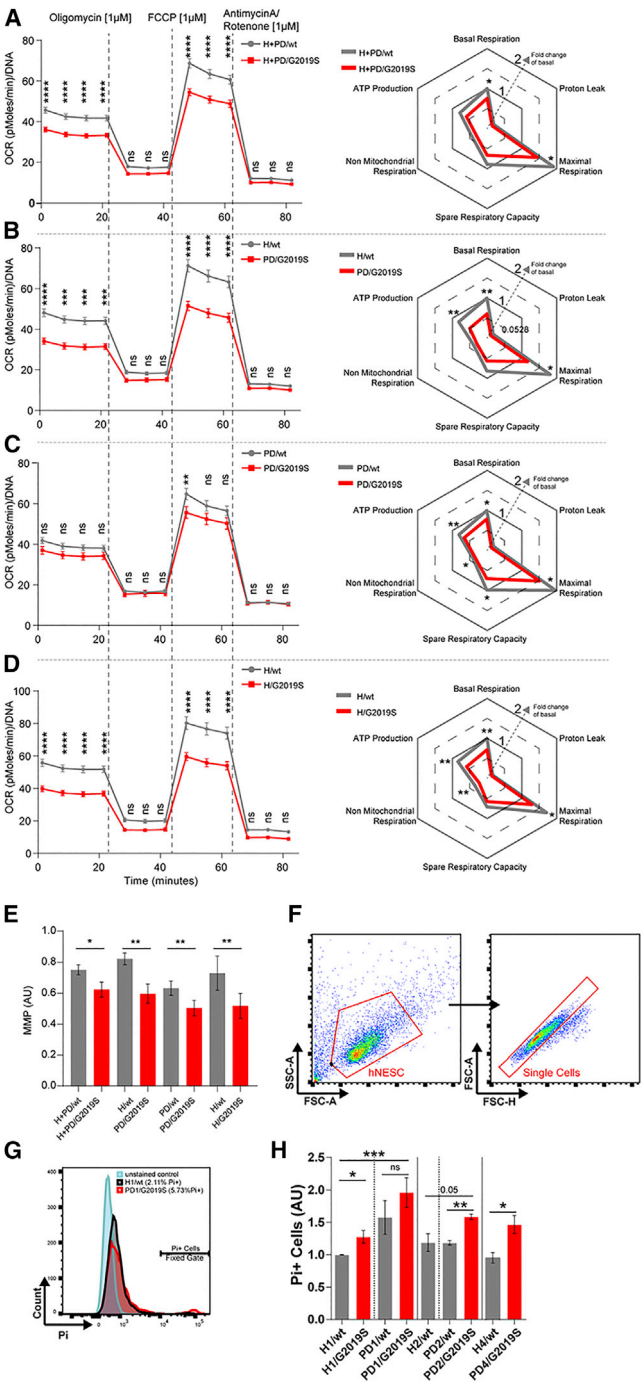

Figure 3. LRRK2-G2019S Induces Loss of Respiratory Capacity and Cell Death

(A–D) Mitochondrial total respiratory capacity measurements obtained using Seahorse, N = 3, n = 8 of the following cell groupings (A) H + PD/WT and H + PD/G2019S, (B) H/WT and PD/G2019S, (C) PD/WT and PD/G2019S, (D) H/WT and H/G2019S. Maximal respiration, proton leakage, basal respiration, ATP production, and non-mitochondrial respiration are represented with OCR graphs shown on the left and with spider plots on the right. Data in the spider plot were calculated based on the grouped data points of the oxygen consumption rates. Significant differences between the groups were tested using a two-way ANOVA, as indicated in the graphs.

(E) Mitochondrial membrane potential (MMP) quantification. The data were normalized to MitoTracker 488 live staining and H1 data. Statistical significance was tested using Student's t-test.

(F–H), (F) Flow cytometry scatter plots showing the gating strategy for the Pi quantification of the NESC population. (G) Representative histograms showing the Pi^+ cell fraction in the H1/WT and PD1/G2019S NESCs. (H) Bar graphs showing the resulting Pi^+ cell quantification in all the applied groupings, , N = 3–4, n = 1. In all panels, the data are presented as the mean ± SEM. N indicates the number of experimental repetitions, n indicates the number of technical replicates per cell line.

different behavior stresses the relevance of NESCs for the study of PD. Comparing PD1/WT with PD1/G2019S, the increase did not reach statistical significance.

Together, these findings suggest that mitochondria are functionally altered in LRRK2-G2019S NESCs and this is associated with increased cell death.

LRRK2-G2019S Triggers Aberrant Mitochondrial Quality Control

Mitochondrial functionality and turnover are ultimately linked. The effective clearance of dysfunctional mitochondria is strongly dependent on the autophagosomal-lysosomal pathway (ALP). The mitochondrial phenotypes we observed in LRRK2-G2019S-expressing NESCs are potentially the result of ineffective mitochondrial clearance, which might be the result of insufficient ALP function (Youle and van der Bliek, 2012). Macromitophagy is ALP mediated (Figure 4A). Thus, we speculated that ALP in LRRK2-G2019S NESCs could be affected, potentially resulting in insufficient mitochondrial clearance. Accordingly, we performed HCS-based lysosome quantification to detect differences in the final and rate-limiting step of ALP.

After unbiased identification of all lysosomal-associated membrane protein 2-positive ($LAMP2^+$) areas in single cells (Figure 4B), we quantified the $LAMP2^+$ puncta representing the total pool of lysosomes, including potential non-acidified pre-lysosomes. We quantified lysosome number and total lysosomal area (Figures 4C, S3A, and S3B). Based on these features, we calculated the mean size of all lysosomes (Figures 4D and S2C). The approach revealed a reduced number of lysosomes, reduced total lysosomal area, and reduced mean lysosomal size in LRRK2-G2019S-expressing NESCs compared with LRRK2-WT. In most comparisons, these lysosomal phenotypes were directly associated with LRRK2-G2019S mutation. However, the results obtained with H/G2019S isogenic controls indicated that LRRK2-G2019S itself is not sufficient to affect the total lysosomal area per NESC feature. We next addressed the potential

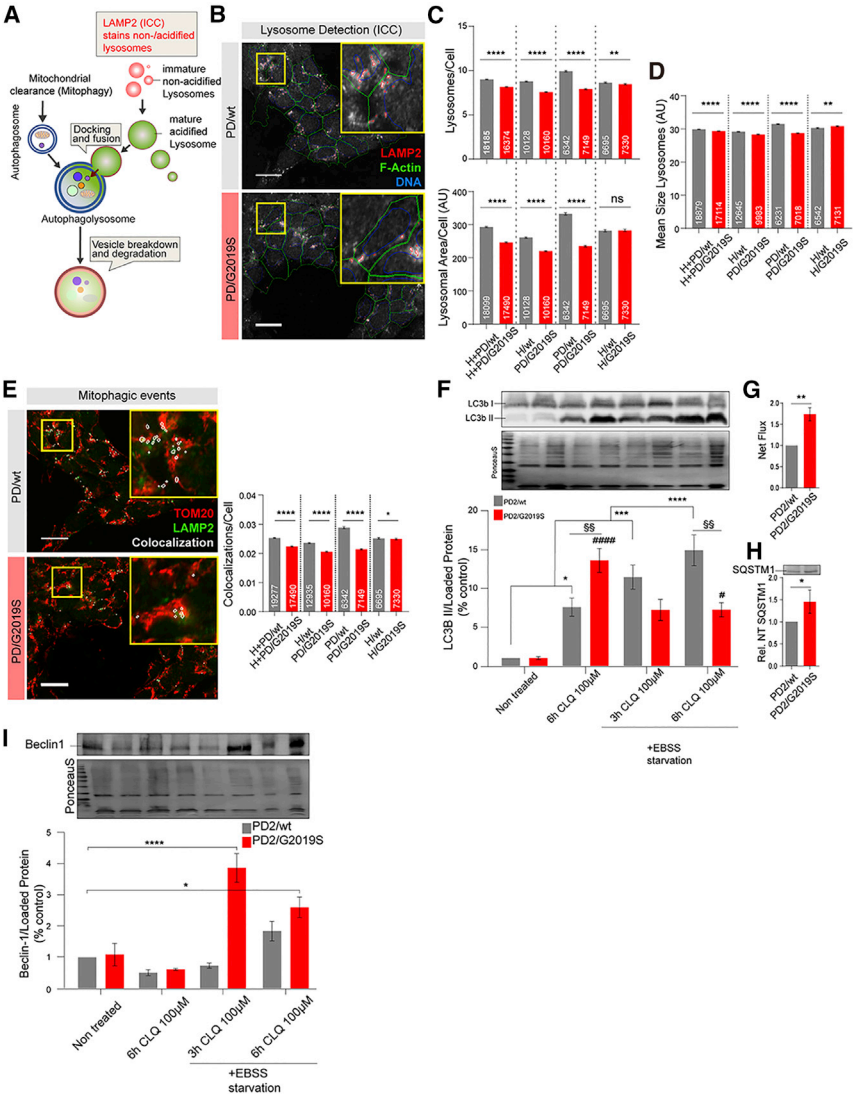

Figure 4. LRRK2-G2019S Impairs Mitochondrial Quality Control

(A) Illustration depicting the mitochondrial clearance pathway via lysosomes (adapted from Fullgrabe et al., 2014), highlighting staining methods and chloroquine perturbation.

(B) Representative photomicrographs of LAMP2 ICC-based lysosome quantification; HCS-based feature detection is indicated.

(C–E) HCS-based quantification of lysosomal morphological features per cell, grouped comparisons (N = 3, n = 3); the number of single cells analyzed is indicated in each bar. Statistical significance was analyzed using Mann-Whitney test. The following parameters were assessed: (C) number of lysosomes and lysosomal area per cell; (D) mean lysosome size per cell; (E) mitophagy level estimation using quantification of lysosomal (LAMP2) and mitochondrial (TOM20) staining co-localization events. Representative TOM20 and LAMP2 photomicrographs are shown with co-localization in white (the co-localization events may be in another z plane). The number of cells analyzed is indicated in the bars.

(F–I) Western blot-based autophagy activity and stress activation analysis in NESCs (N = 3, n = 3). Statistical significance was determined using two-way ANOVA and Tukey multiple comparisons test (*comparison with untreated PD2.GC cells; #comparison with untreated PD2.G2019S cells; and §comparison with PD2.GC cells—same condition). (F) Quantification of LC3B I/II protein levels under basal conditions and during blocking of autophagosomal-lysosomal fusion (CLQ, chloroquine) in combination with activation of autophagy using Earle's balanced salt solution-based starvation. (G) Calculation of net flux autophagic activity. (H) Relative basal SQSTM1 protein levels. (I) Upstream autophagy activation signal analysis using Beclin-1. Scale bars, 20 µm. For all panels, the data are presented as the mean ± SEM. N indicates the number of experimental repetitions, n indicates the number of technical replicates per cell line.

mitophagy events by quantifying the co-localization of LAMP2 puncta with the mitochondrial TOM20 area in single NESCs (Figures 4E and S2D). We detected a significantly reduced number of co-localization in LRRK2-G2019S-expressing NESCs compared with controls, indicating reduced macro-mitophagic clearance via lysosomes.

To investigate the potential dysregulation of the ALP upstream of the lysosome, we performed a protein-based analysis of autophagosomal capacity using cells of one patient and its isogenic control (PD2/WT and PD2/G2019S). Using western blotting analysis (Figures 4F–4I), we measured the protein levels of the autophagosomal membrane-bound form of LC3B (LC3B-II) (Figure 4F), sequestesome 1 (SQSTM1, also known as p62) (Figures 4H and S3E), and Beclin-1 (Figure 4I), widely used markers for monitoring the autophagic process, in the absence or in the presence of chloroquine, an inhibitor of ALP degradation.

We observed significantly elevated basal autophagic flux activity in LRRK2-G2019S-expressing NESCs compared with LRRK2-WT (Figure 4G). Consistently, the autophagy substrate SQSTM1 levels were elevated in these cells (Figures 4H and S3G). Next, we tested the cellular autophagy response to Earle's balanced salt solution-induced starvation. Despite the observed elevated basal autophagic level

in the patient cells, these levels were not sustained during starvation (Figure 4F). Although starvation resulted in continuously elevated LC3BII levels in controls, the presence of CLQ, the LC3BII levels in LRRK2-G2019S-expressing NESCs were markedly decreased compared with controls. Strikingly, parallel quantification of Beclin-1 (Figure 4I), which acts upstream of autophagy signaling and activation (Kang et al., 2011), indicated a strong activation signal, as reflected by elevated Beclin-1 levels (3 and 6 h) and in the presence of CLQ 100 μM. However, the Beclin-1 signal did not result in autophagosome formation because of the lack of LC3BII abundance under the same conditions (Figure 4I). These results show that LRRK2-G2019S negatively affects autophagy upstream of the observed lysosomal limitations.

Collectively, the ALP analysis of NESCs revealed decreased ALP functionality in LRRK2-G2019S-expressing NESCs compared with isogenic controls.

DISCUSSION

In this study, we observed that mitochondria in NESC cells carrying the LRRK2-G2019S mutation were more fragmented and were more prone to release ROS compared with isogenic controls. Beside morphology, also the functionality of mitochondria was impaired in the presence of LRRK2-G2019S, as shown by the decreased membrane potential and respiratory capacity.

Evidence from human neurons has previously shown that LRRK2 influences mitochondrial function (Cooper et al., 2012; Sanders et al., 2014) and dynamics (Wang et al., 2012). An increase of fragmented mitochondria has been observed in iPSC-derived dopaminergic neurons along with impaired clearance of unhealthy mitochondria, and alteration in mitochondria respiration and bioenergetics, as reviewed in Sison et al. (2018). However, no information was previously available regarding the status of the mitochondria at the stem cell level in the context of LRRK2. Here, we showed that already before neuronal differentiation at the level of NESCs, mitochondrial phenotypes are detectable, suggesting that this is a relevant model to study PD mitochondrial alterations. Moreover, mitochondria were recently shown to be of crucial importance in neural stem cells (Lorenz et al., 2017; Sanders et al., 2014), highlighting their key role in cell fate decisions during development (Beckervordersandforth et al., 2017; Khacho et al., 2016). Mitochondria are critically involved in numerous cellular processes that rely on energy, such as cell growth, maintenance, proliferation, activity, and neurogenesis (Beckervordersandforth et al., 2017). Based on these findings, it is tempting to speculate that the described mitochondrial alterations in NESCs are important contributors to the PD-specific dynamics of dopaminergic differentiation.

Neurogenic niches are characterized by particularly elevated metabolic activity, which associates with high ROS levels (Walton et al., 2012). Beside their detrimental effect on cell viability, ROS play a role in the regulation of neural cell fate (Khacho et al., 2016; Orford and Scadden, 2008; Sarsour et al., 2009). Consequently, the observed elevated ROS levels might contribute to the increased cell death observed in LRRK2-G2019S NESCs. LRRK2 mutation can alter the interaction with the antioxidant protein peroxiredoxin 3, reducing the ability to scavenge ROS (Angeles et al., 2011). It has been shown that mitochondria-targeted antioxidants effectively sequester ROS and protect against mitochondrial damage (Oyewole and Birch-Machin, 2015). NESCs are stable and highly proliferative cultures, which permit quick evaluation of functional and morphological mitochondrial features. The present model and the here-described assays can leverage pharmacological screenings that aim to ameliorate bioenergetics defects and reduce mitochondrial ROS in the context of PD.

Control of mitochondrial homeostasis is of major importance in cellular homeostasis (Dias et al., 2013). Insufficient clearance of dysfunctional mitochondria is associated with accumulation of damaged mitochondria and high ROS levels, ultimately resulting in reduced cell viability. Clearance of malfunctioning mitochondria largely occurs through lysosomal-mediated mitophagy. Lysosomal dysfunctionality has been associated to PD in several studies (Chang et al., 2017; Roosen and Cookson, 2016). The status of mitochondrial biogenesis can be directly linked to the functionality of mitochondrial quality control mechanisms (Tronstad et al., 2014). Lysosomal phenotypes in PD context have mostly been described in terminally differentiated neurons (Migdalska-Richards et al., 2017). Here, we also found LRRK2-G2019S-associated alterations in the ALP in NESCs, indicating that ALP dysregulation can already occur at a developmental stage.

In summary, the data presented in this study highlight disease-specific phenotypes of patient-derived NESCs carrying the LRRK2-G2019S mutation. The detection of these phenotypes in a developmentally early neural stem cell model supports the hypothesis that PD might have a developmental component.

EXPERIMENTAL PROCEDURES

The work with human iPSCs was approved by the local ethical committee (Ethic Review Panel of the University of Luxembourg, PDiPS project and CNER No 201305/04).

Single-Cell RNA-Seq Using Drop-Seq

Microfluidics Fabrication

Microfluidics devices were fabricated using a previously published design (Macosko et al., 2015). Soft lithography was performed

using previously published protocols using SU-8 2050 photoresist (MicroChem) on a 4″ silicon substrate (Macosko et al., 2015; Mazutis et al., 2013). Drop-seq chips were fabricated using silicon-based polymerization chemistry. In brief, a polydimethylsiloxane (PDMS) base and a crosslinker (Dow Corning), were combined at a 10:1 ratio, mixed, and degassed, before pouring the mix onto the Drop-seq master template. PDMS was cured on the master template, at 80°C for 2 h. After the incubation and cooling, the PDMS stamps were cut and the inlet/outlet ports were punched with 1.25-mm biopsy punchers (World Precision Instruments). The PDMS monolith was plasma-bonded to a clean microscopic glass slide using Harrick plasma cleaner. The flow channels of the Drop-seq chip were then subject to hydrophobicity treatment.

Single-Cell Suspension and RNA-Seq

The key steps of the protocol used here align with the original Drop-seq work (Macosko et al., 2015) with minor changes as described below. After the enzymatic digestion of the cells using Accutase at 37°C (10–20 min) single cells were pelleted by centrifugation at 300 rcf for 5 min. Cell clumps and debris were excluded from the suspension using a 40-μm nylon cell strainer (BD). The single-cell suspension was diluted with 1% BSA in 1× PBS to achieve a cell density of ~150 cells/mL. Diluted cells were placed on ice until loaded onto the pre-fabricated Drop-seq chip. Specially synthesized barcoded beads (ChemGenes) were co-encapsulated with cells inside the droplets, having optimized lysis reagents adapted from Macosko et al. (2015). This procedure allows capturing the cellular mRNA by barcoded oligo (dT) handles on the surface of the specialized beads. The microfluidic chip generates monodispersed droplets of ~1 nL volume. The bead concentration used for optimal single bead encapsulation within the droplet was 200 beads/mL, and beads were prepared in Drop-seq lysis buffer (Macosko et al., 2015).

One ml of the cell and the bead suspension was loaded into 3-mL syringes (BD). A micro-stirrer was used (V&P Scientific) to keep the beads in stable suspension. The QX200 carrier oil (Bio-Rad) was used as a continuous phase in the droplet generation. Oil was loaded into a 20-mL syringe (BD). For droplet generation, 3.6 and 13 mL/h were used for the dispersed and continuous phases, respectively, using KD Scientific Legato syringe pumps. This generated droplets with a diameter of ~115 μm (~1 nL volume). The droplet suspension was collected in a 50-mL Falcon tube. Then, the droplet consistency and stability were documented by bright-field microscopy to check on multiple bead occupancy.

The subsequent droplet breakage, reverse transcription, and the exonuclease treatment were carried out in accordance with the original Drop-seq work (Macosko et al., 2015). The buffer for the reverse transcription contained: 1× Maxima RT buffer, 4% Ficoll PM 400 (Sigma), 1 μM dNTPs (Thermo Scientific), 1 U/mL RNase Inhibitor (Lucigen), 2.5 μM Template Switch Oligo, and 10 U/mL Maxima H Minus RT (Thermo Scientific).

Following Exo I treatment, the bead counts were estimated using an INCYTO C-Chip disposable hemacytometer. Then, aliquots of 10,000 beads were prepared in 0.2-mL Eppendorf PCR tubes. PCR mix was dispensed in a volume of 50 mL using 1× Hifi HotStart ReadyMix (Kapa Biosystems) and 0.8 mM Template-Switch-PCR primer. The thermocycling program for the PCR amplification was adapted from the previous work, except for the final PCR cycles: 95°C for 3 min; four cycles of: 98°C for 20 s, 65°C for 45 s, 72°C for 3 min; 10 cycles of: 98°C for 20 s, 67°C for 20 s, 72°C for 3 min; followed by a final extension step of 72°C for 5 min. After PCR amplification, libraries were purified with 0.6× Agencourt AMPure XP beads (Beckman Coulter), in accordance with the manufacturer's protocol. Finally, the purified libraries were eluted in 20 μL of molecular-grade water. Before the sequencing library preparation, the quality and the concentration of the libraries was assessed using Bioanalyzer High Sensitivity Chip (Agilent Technologies).

3D Blinded Unbiased Mitochondrial Morphology Analysis

3D image processing and analysis based on LSM confocal z stacks were performed using Image-Pro Plus software (version 7.0) with SharpStack Total deconvolution and 3D Constructor modules (Media Cybernetics, Washington, USA). Analysis of mitochondrial shape properties was conducted by adapting previously described protocols (Nikolaisen et al., 2014). The mitochondrial channel of the confocal z stack was extracted, background-corrected (fixed level), and spatially calibrated and 3D blind deconvolution (10 iterations) was performed. Flat 2D projections (maximum intensity composite) of the mitochondrial z stacks were employed for manual segmentation of single cells, but we also compared with the nuclear and cytoplasmic channels (F-actin) as guidance in this step. By drawing the cellular outline, a binary black and white image was created, and this was subsequently used as a mask for making a z stack with only one (or two) cell(s). The processed single-cell z stacks were loaded into the 3D Constructor module using no sub-sampling, and an isosurface (surface level = 900) was created without further filtering or simplification. Mitochondrial shape-parameters were then obtained and analyzed. Objects larger than 0.02 μm^3 were quantified as mitochondrial objects.

The quantitative image analysis was done with blinded samples. Pooled single-cell data obtained from three replicated experiments are presented. The inter-experimental variation was evaluated and found insignificant (not shown). Statistical analysis of two groups was performed using t test. Only cells that were possible to segment into single cells or doublets (only a few cases) were included in this analysis. For doublets, the mean value was used for statistical analysis. Cells that were clearly apoptotic (condensed nucleus, fragmented cell body) were excluded. Samples in this analysis (n = number of cells analyzed): PD1.G2019S n = 69, PD1.GC: n = 90, H1.G2019S: n = 72, H1: n = 66.

Quantification and Statistical Analysis

Statistical analysis was performed as follows: unpaired or paired (isogenic controls) Student's t test when the sample size was small and data normally distributed. For HCS imaging data that was not normally distributed we applied Mann-Whitney test. Two-way ANOVA followed by Bonferroni test was applied when indicated. All data are presented as mean ± SEM. Significance levels were set at *$p < 0.05$, **$p < 0.01$, ***$p < 0.001$, ****$p < 0.0001$.

For plotting, GraphPad Prism was used. For single-cell RNA-seq data, the statistical significance of the differences in cumulative

gene expressions (Figure 1C) was assessed using a z test, with Bonferroni correction to account for multiple testing. More details on the different statistical analyses of single-cell RNA-seq data are explained in the section titled "Analysis of Mitochondrial genes expression at the single cell level" of the Supplemental Information.

ACCESSION NUMBERS

The accession number for the FASQT files reported in this paper is number GEO: GSE128040.

SUPPLEMENTAL INFORMATION

Supplemental Information can be found online at https://doi.org/10.1016/j.stemcr.2019.03.004.

AUTHOR CONTRIBUTIONS

Conceptualization, J.W. and J.C.S.; Cell Culture and Assay Design, J.W.; Methodology, J.W., P.M.A.A., S.L.N., S.K.P., L.S., S.M., R.P., F.H., X.Q., J.J, J.A.-F, T.I., A.M., L.G.C., S.B., A.S., D.G., T.S., and K.J.T.; Investigation, J.W., P.M.A.A., S.N., S.K.P., S.B., S.M., R.P., F.H., A.S., and K.J.T.; Writing – Original Draft, S.B., J.W., and J.C.S.; Writing – Review & Editing, all the co-authors; Supervision, L.P.D.A., A.S., K.J.T., and J.C.S.; J.W. and S.B. contributed equally; P.M.A.A., S.L.N., and S.K.B. contributed equally.

ACKNOWLEDGMENTS

The authors would like to thank Thea van Wuellen, Marie Fossepre, Antoine Treff, and Annegraet Daujeumont for technical assistance. We thank Prof. Dr. Hans R. Schöler (Max-Planck-Gesellschaft), Dr. Jared Sterneckert (CRTD), Prof. Dr. Thomas Gasser (Hertie Institute in Tuebingen), and the Coriell Institute for providing the cell lines. The LAMP-2 monoclonal antibody was developed by J.T. August and J.E.K. Hildreth and was obtained from the Developmental Studies Hybridoma Bank created by the NICHD of the NIH and maintained at the University of Iowa, Department of Biology, Iowa City, IA 52242, USA. This project was supported by the LCSB pluripotent stem cell core facility. The JCS lab is supported by the Fonds National de la Recherche (FNR) (CORE, C13/BM/5791363 and Proof-of-Concept program PoC15/11180855 & PoC16/11559169). This is an EU Joint Programme - Neurodegenerative Disease Research (JPND) project (INTER/JPND/14/02; INTER/JPND/15/11092422). Further support comes from the SysMedPD project, which has received funding from the European Union's Horizon 2020 research and innovation program under grant agreement no. 668738. J.W., X.Q., L.G.-C., J.J., and A.S.M. were supported by fellowships from the FNR (AFR, Aides à la Formation-Recherche). S.M. is supported by the FNR through the PRIDE DTU CriTiCS, reference 10907093. We also thank the private donors who support our work at the LCSB.

Received: November 9, 2018
Revised: March 14, 2019
Accepted: March 14, 2019
Published: April 11, 2019

REFERENCES

Angeles, D.C., Gan, B.H., Onstead, L., Zhao, Y., Lim, K.L., Dachsel, J., Melrose, H., Farrer, M., Wszolek, Z.K., Dickson, D.W., et al. (2011). Mutations in LRRK2 increase phosphorylation of peroxiredoxin 3 exacerbating oxidative stress-induced neuronal death. Hum. Mutat. *32*, 1390–1397.

Beckervordersandforth, R., Ebert, B., Schaffner, I., Moss, J., Fiebig, C., Shin, J., Moore, D.L., Ghosh, L., Trinchero, M.F., Stockburger, C., et al. (2017). Role of mitochondrial metabolism in the control of early lineage progression and aging phenotypes in adult hippocampal neurogenesis. Neuron *93*, 1518.

Brand, M.D., and Nicholls, D.G. (2011). Assessing mitochondrial dysfunction in cells. Biochem. J. *435*, 297–312.

Burbulla, L.F., and Kruger, R. (2011). Converging environmental and genetic pathways in the pathogenesis of Parkinson's disease. J. Neurol. Sci. *306*, 1–8.

Calvo, S.E., Clauser, K.R., and Mootha, V.K. (2016). MitoCarta2.0: an updated inventory of mammalian mitochondrial proteins. Nucleic Acids Res. *44*, D1251–D1257.

Chang, D., Nalls, M.A., Hallgrimsdottir, I.B., Hunkapiller, J., van der Brug, M., Cai, F., International Parkinson's Disease Genomics, C., Me Research, T., Kerchner, G.A., Ayalon, G., et al. (2017). A meta-analysis of genome-wide association studies identifies 17 new Parkinson's disease risk loci. Nat. Genet. *49*, 1511–1516.

Conti, L., Pollard, S.M., Gorba, T., Reitano, E., Toselli, M., Biella, G., Sun, Y., Sanzone, S., Ying, Q.L., Cattaneo, E., et al. (2005). Niche-independent symmetrical self-renewal of a mammalian tissue stem cell. PLoS Biol. *3*, e283.

Cookson, M.R. (2016). Cellular functions of LRRK2 implicate vesicular trafficking pathways in Parkinson's disease. Biochem. Soc. Trans. *44*, 1603–1610.

Cooper, O., Seo, H., Andrabi, S., Guardia-Laguarta, C., Graziotto, J., Sundberg, M., McLean, J.R., Carrillo-Reid, L., Xie, Z., Osborn, T., et al. (2012). Pharmacological rescue of mitochondrial deficits in iPSC-derived neural cells from patients with familial Parkinson's disease. Sci. Transl. Med. *4*, 141ra190.

Dias, V., Junn, E., and Mouradian, M.M. (2013). The role of oxidative stress in Parkinson's disease. J. Parkinsons Dis. *3*, 461–491.

Fullgrabe, J., Klionsky, D.J., and Joseph, B. (2014). The return of the nucleus: transcriptional and epigenetic control of autophagy. Nat. Rev. Mol. Cell Biol. *15*, 65–74.

Funayama, M., Hasegawa, K., Kowa, H., Saito, M., Tsuji, S., and Obata, F. (2002). A new locus for Parkinson's disease (PARK8) maps to chromosome 12p11.2-q13.1. Ann. Neurol. *51*, 296–301.

Gonzalez-Cano, L., Menzl, I., Tisserand, J., Nicklas, S., and Schwamborn, J.C. (2018). Parkinson's disease-associated mutant LRRK2-mediated inhibition of miRNA activity is antagonized by TRIM32. Mol. Neurobiol. *55*, 3490–3498.

Haddad, D., and Nakamura, K. (2015). Understanding the susceptibility of dopamine neurons to mitochondrial stressors in Parkinson's disease. FEBS Lett. *589*, 3702–3713.

Hsieh, C.H., Shaltouki, A., Gonzalez, A.E., Bettencourt da Cruz, A., Burbulla, L.F., St Lawrence, E., Schule, B., Krainc, D., Palmer, T.D., and Wang, X. (2016). Functional impairment in miro degradation

and mitophagy is a shared feature in familial and sporadic Parkinson's disease. Cell Stem Cell *19*, 709–724.

Igathinathane, C., Pordesimo, L.O., Columbus, E.P., Batchelor, W.D., and Methuku, S.R. (2008). Shape identification and particles size distribution from basic shape parameters using ImageJ. Comput. Electron. Agric. *63*, 168–182.

Kang, R., Zeh, H.J., Lotze, M.T., and Tang, D. (2011). The Beclin 1 network regulates autophagy and apoptosis. Cell Death Differ. *18*, 571–580.

Khacho, M., Clark, A., Svoboda, D.S., Azzi, J., MacLaurin, J.G., Meghaizel, C., Sesaki, H., Lagace, D.C., Germain, M., Harper, M.E., et al. (2016). Mitochondrial dynamics impacts stem cell identity and fate decisions by regulating a nuclear transcriptional program. Cell Stem Cell *19*, 232–247.

Klein, C., and Westenberger, A. (2012). Genetics of Parkinson's disease. Cold Spring Harb. Perspect. Med. *2*, a008888.

Krumova, P., Reyniers, L., Meyer, M., Lobbestael, E., Stauffer, D., Gerrits, B., Muller, L., Hoving, S., Kaupmann, K., Voshol, J., et al. (2015). Chemical genetic approach identifies microtubule affinity-regulating kinase 1 as a leucine-rich repeat kinase 2 substrate. FASEB J. *29*, 2980–2992.

Lambeth, J.D., Kawahara, T., and Diebold, B. (2007). Regulation of Nox and Duox enzymatic activity and expression. Free Radic. Biol. Med. *43*, 319–331.

Lesage, S., Durr, A., and Brice, A. (2007). LRRK2: a link between familial and sporadic Parkinson's disease? Pathol. Biol. (Paris) *55*, 107–110.

Liu, G.H., Qu, J., Suzuki, K., Nivet, E., Li, M., Montserrat, N., Yi, F., Xu, X., Ruiz, S., Zhang, W., et al. (2012). Progressive degeneration of human neural stem cells caused by pathogenic LRRK2. Nature *491*, 603–607.

Lorenz, C., Lesimple, P., Bukowiecki, R., Zink, A., Inak, G., Mlody, B., Singh, M., Semtner, M., Mah, N., Aure, K., et al. (2017). Human iPSC-derived neural progenitors are an effective drug discovery model for neurological mtDNA disorders. Cell Stem Cell *20*, 659–674.e9.

Macosko, E.Z., Basu, A., Satija, R., Nemesh, J., Shekhar, K., Goldman, M., Tirosh, I., Bialas, A.R., Kamitaki, N., Martersteck, E.M., et al. (2015). Highly parallel genome-wide expression profiling of individual cells using nanoliter droplets. Cell *161*, 1202–1214.

Mazutis, L., Gilbert, J., Ung, W.L., Weitz, D.A., Griffiths, A.D., and Heyman, J.A. (2013). Single-cell analysis and sorting using droplet-based microfluidics. Nat. Protoc. *8*, 870–891.

Migdalska-Richards, A., Wegrzynowicz, M., Rusconi, R., Deangeli, G., Di Monte, D.A., Spillantini, M.G., and Schapira, A.H.V. (2017). The L444P Gba1 mutation enhances alpha-synuclein induced loss of nigral dopaminergic neurons in mice. Brain *140*, 2706–2721.

Narendra, D., Tanaka, A., Suen, D.F., and Youle, R.J. (2008). Parkin is recruited selectively to impaired mitochondria and promotes their autophagy. J. Cell Biol. *183*, 795–803.

Nikolaisen, J., Nilsson, L.I., Pettersen, I.K., Willems, P.H., Lorens, J.B., Koopman, W.J., and Tronstad, K.J. (2014). Automated quantification and integrative analysis of 2D and 3D mitochondrial shape and network properties. PLoS One *9*, e101365.

Orford, K.W., and Scadden, D.T. (2008). Deconstructing stem cell self-renewal: genetic insights into cell-cycle regulation. Nat. Rev. Genet. *9*, 115–128.

Oyewole, A.O., and Birch-Machin, M.A. (2015). Mitochondria-targeted antioxidants. FASEB J. *29*, 4766–4771.

Ozelius, L.J., Senthil, G., Saunders-Pullman, R., Ohmann, E., Deligtisch, A., Tagliati, M., Hunt, A.L., Klein, C., Henick, B., Hailpern, S.M., et al. (2006). LRRK2 G2019S as a cause of Parkinson's disease in Ashkenazi Jews. N. Engl. J. Med. *354*, 424–425.

Paisan-Ruiz, C., Jain, S., Evans, E.W., Gilks, W.P., Simon, J., van der Brug, M., Lopez de Munain, A., Aparicio, S., Gil, A.M., Khan, N., et al. (2004). Cloning of the gene containing mutations that cause PARK8-linked Parkinson's disease. Neuron *44*, 595–600.

Pissadaki, E.K., and Bolam, J.P. (2013). The energy cost of action potential propagation in dopamine neurons: clues to susceptibility in Parkinson's disease. Front. Comput. Neurosci. *7*, 13.

Reinhardt, P., Glatza, M., Hemmer, K., Tsytsyura, Y., Thiel, C.S., Hoing, S., Moritz, S., Parga, J.A., Wagner, L., Bruder, J.M., et al. (2013). Derivation and expansion using only small molecules of human neural progenitors for neurodegenerative disease modeling. PLoS One *8*, e59252.

Roosen, D.A., and Cookson, M.R. (2016). LRRK2 at the interface of autophagosomes, endosomes and lysosomes. Mol. Neurodegener. *11*, 73.

Sanders, L.H., Laganiere, J., Cooper, O., Mak, S.K., Vu, B.J., Huang, Y.A., Paschon, D.E., Vangipuram, M., Sundararajan, R., Urnov, F.D., et al. (2014). LRRK2 mutations cause mitochondrial DNA damage in iPSC-derived neural cells from Parkinson's disease patients: reversal by gene correction. Neurobiol. Dis. *62*, 381–386.

Sarsour, E.H., Kumar, M.G., Chaudhuri, L., Kalen, A.L., and Goswami, P.C. (2009). Redox control of the cell cycle in health and disease. Antioxid. Redox Signal. *11*, 2985–3011.

Schapira, A.H., Cooper, J.M., Dexter, D., Clark, J.B., Jenner, P., and Marsden, C.D. (1990). Mitochondrial complex I deficiency in Parkinson's disease. J. Neurochem. *54*, 823–827.

Sison, S.L., Vermilyea, S.C., Emborg, M.E., and Ebert, A.D. (2018). Using patient-derived induced pluripotent stem cells to identify Parkinson's disease-relevant phenotypes. Curr. Neurol. Neurosci. Rep. *18*, 84.

Smith, G.A., Jansson, J., Rocha, E.M., Osborn, T., Hallett, P.J., and Isacson, O. (2016). Fibroblast biomarkers of sporadic Parkinson's disease and LRRK2 kinase inhibition. Mol. Neurobiol. *53*, 5161–5177.

Trimmer, P.A., Swerdlow, R.H., Parks, J.K., Keeney, P., Bennett, J.P., Jr., Miller, S.W., Davis, R.E., and Parker, W.D., Jr. (2000). Abnormal mitochondrial morphology in sporadic Parkinson's and Alzheimer's disease cybrid cell lines. Exp. Neurol. *162*, 37–50.

Tronstad, K.J., Nooteboom, M., Nilsson, L.I., Nikolaisen, J., Sokolewicz, M., Grefte, S., Pettersen, I.K., Dyrstad, S., Hoel, F., Willems, P.H., et al. (2014). Regulation and quantification of cellular mitochondrial morphology and content. Curr. Pharm. Des. *20*, 5634–5652.

Turrens, J.F. (2003). Mitochondrial formation of reactive oxygen species. J. Physiol. *552*, 335–344.

Tysnes, O.B., and Storstein, A. (2017). Epidemiology of Parkinson's disease. J. Neural Transm. (Vienna) *124*, 901–905.

Vitte, J., Traver, S., Maues De Paula, A., Lesage, S., Rovelli, G., Corti, O., Duyckaerts, C., and Brice, A. (2010). Leucine-rich repeat kinase 2 is associated with the endoplasmic reticulum in dopaminergic neurons and accumulates in the core of Lewy bodies in Parkinson disease. J. Neuropathol. Exp. Neurol. *69*, 959–972.

Wallings, R., Manzoni, C., and Bandopadhyay, R. (2015). Cellular processes associated with LRRK2 function and dysfunction. FEBS J. *282*, 2806–2826.

Walton, N.M., Shin, R., Tajinda, K., Heusner, C.L., Kogan, J.H., Miyake, S., Chen, Q., Tamura, K., and Matsumoto, M. (2012). Adult neurogenesis transiently generates oxidative stress. PLoS One *7*, e35264.

Wang, X., Yan, M.H., Fujioka, H., Liu, J., Wilson-Delfosse, A., Chen, S.G., Perry, G., Casadesus, G., and Zhu, X. (2012). LRRK2 regulates mitochondrial dynamics and function through direct interaction with DLP1. Hum. Mol. Genet. *21*, 1931–1944.

West, A.B., Moore, D.J., Biskup, S., Bugayenko, A., Smith, W.W., Ross, C.A., Dawson, V.L., and Dawson, T.M. (2005). Parkinson's disease-associated mutations in leucine-rich repeat kinase 2 augment kinase activity. Proc. Natl. Acad. Sci. U S A *102*, 16842–16847.

Wu, S., Zhou, F., Zhang, Z., and Xing, D. (2011). Mitochondrial oxidative stress causes mitochondrial fragmentation via differential modulation of mitochondrial fission-fusion proteins. FEBS J. *278*, 941–954.

Youle, R.J., and van der Bliek, A.M. (2012). Mitochondrial fission, fusion, and stress. Science *337*, 1062–1065.

Stem Cell Reports, Volume *12*

Supplemental Information

Neural Stem Cells of Parkinson's Disease Patients Exhibit Aberrant Mitochondrial Morphology and Functionality

Jonas Walter, Silvia Bolognin, Paul M.A. Antony, Sarah L. Nickels, Suresh K. Poovathingal, Luis Salamanca, Stefano Magni, Rita Perfeito, Fredrik Hoel, Xiaobing Qing, Javier Jarazo, Jonathan Arias-Fuenzalida, Tomasz Ignac, Anna S. Monzel, Laura Gonzalez-Cano, Luis Pereira de Almeida, Alexander Skupin, Karl J. Tronstad, and Jens C. Schwamborn

Supplemental Information

Neural stem cells of Parkinson's disease patients exhibit aberrant mitochondrial morphology and functionality

Jonas Walter[1,9], Silvia Bolognin[1,9], Paul M.A. Antony[1,7], Sarah L. Nickels[1,2,7], Suresh K. Poovathingal[1,7,#], Luis Salamanca[1], Stefano Magni[1], Rita Perfeito[3], Fredrik Hoel[4], Xiaobing Qing[1], Javier Jarazo[1], Jonathan Arias-Fuenzalida[1], Tomasz Ignac[1], Anna S. Monzel[1], Laura Gonzalez-Cano[1], Luis Pereira de Almeida[3,5], Alexander Skupin[1,6], Karl J. Tronstad[4], Jens C. Schwamborn[1,8*]

[1] Luxembourg Centre for Systems Biomedicine (LCSB), University of Luxembourg, L-4362 Belvaux, Luxembourg
[2] Life Science Research Unit (LSRU), University of Luxembourg, L-4362 Belvaux, Luxembourg
[3] CNC-Center for Neuroscience and Cell Biology, University of Coimbra, Rua Larga, Coimbra 3004-504, Portugal
[4] Department of Biomedicine, University of Bergen, 5020 Bergen, Norway
[5] Faculty of Pharmacy, University of Coimbra, Coimbra 3000-548, Portugal
[6] Center for Research of Biological Systems, University of California San Diego, La Jolla, CA 92093, USA
[7] These authors contributed equally to this work.
[8] Lead contact
[9] Equal first author contribution
[#] Current address: Single Cell Analytics & Microfluidics Core, VIB-KU Leuven, Herestraat 49, 3000 Leuven, Belgium
* Correspondence: jens.schwamborn@uni.lu (J.C.S.)

Supplemental Figures and Legends

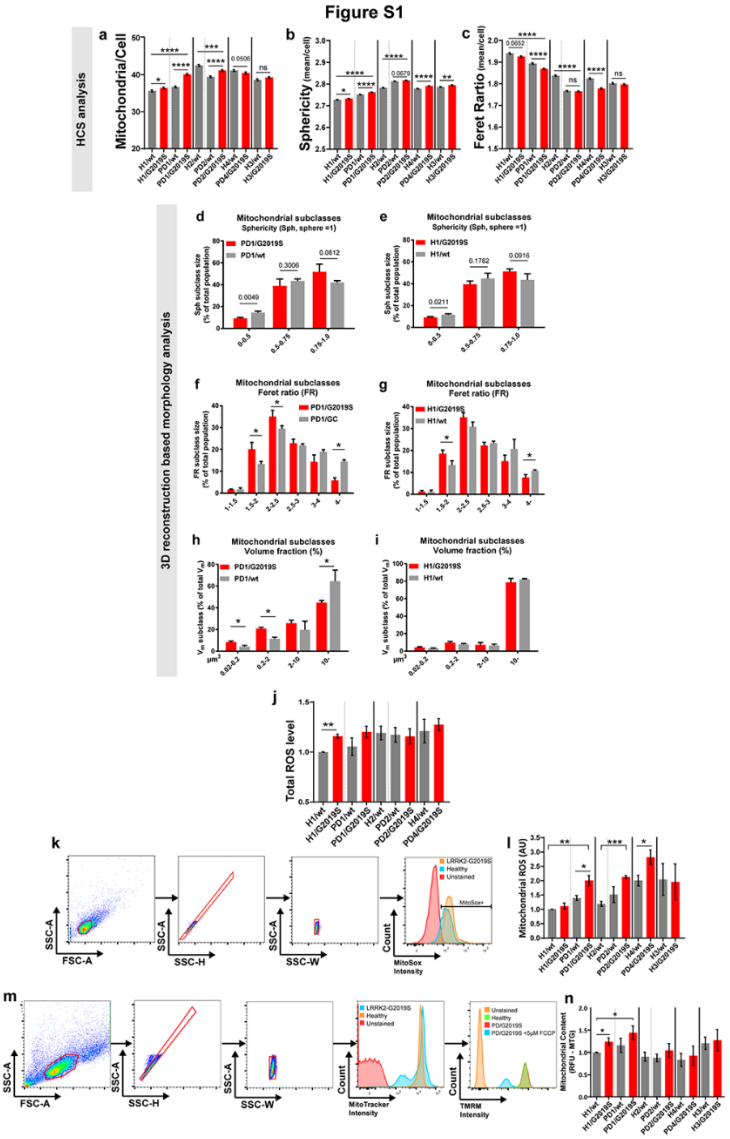

Figure S1. LRRK2-G2019S induces mitochondrial morphological alterations in NESC. Related to Figure 2.

(a-c) Graphs showing HCS-based mitochondrial morphometric analyses before the pooling described in **Figures 1a-c**. Statistical significance was assessed with Mann-Whitney test, N=3, n=3. **(d-i)** 3D mitochondrial morphology analysis (**Figures 1e-j**) in more detailed subclass comparison of: **(d-e)** mitochondrial volume; **(f-g)** Feret ratio; **(h-i)** mitochondrial sphericity, always comparing PD1 and H1 separately. Statistical significance tested via Student's t-test, N=3, n=3. **(j)** Total ROS levels before the described pooling (**Figure 2k**), data normalized to H1, statistical significance tested via Student's t-test, N=5-6, n=3. **(k)** Example gating of flow cytometric of MitoSox (mitochondrial ROS) analysis (**Figures 1l, S1l**) showing all the gating combinations used, and the sample distribution in comparison to unstained control. **(l)** Mitochondrial ROS levels before the described pooling (**Figure 2l**), data normalized to H1, statistical significance tested via Student's t-test, N=4, n=1. **(m)** Example gating of flow cytometry MitoTracker/TMRM analysis showing all the gating combinations used, and the sample distribution in comparison to unstained control. **(n)** Graphs of mitochondrial content analysis using MitoTracker 488 relative fluorescence (RFU), data normalized to H1, significances tested via Student's t-test, N=4, n=2. For all panels, the data are presented as the mean ± SEM. N indicates the number of experimental repetitions, n indicates the number of technical replicates per cell line.

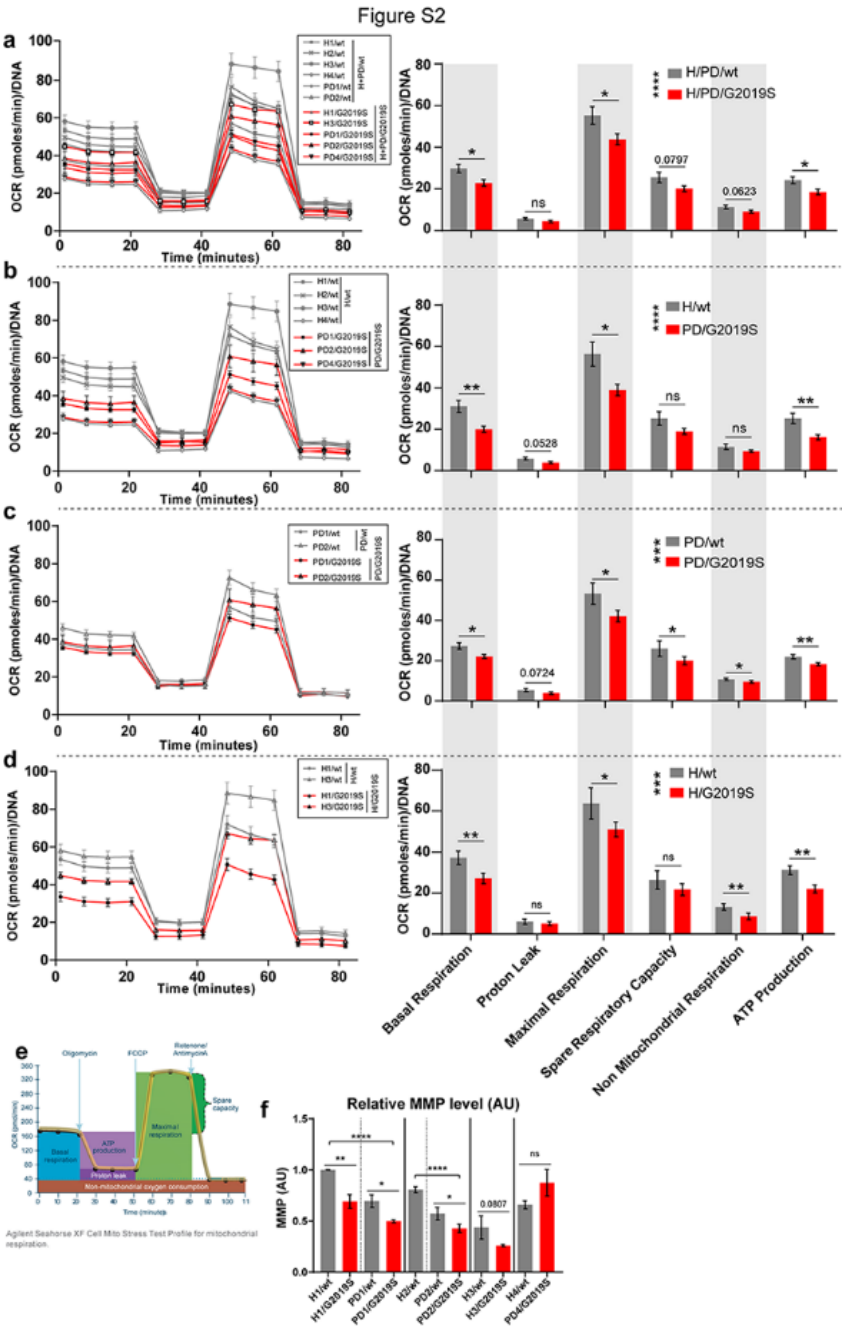

Figure S2. LRRK2-G2019S alters the oxygen consumption rate in NESCs. Related to Figure 3.

(a-d) Graphs showing OCR before the pooling described in **Figure 2a-d**. The OCR graphs on the left show the oxygen consumption over time. The bar graphs on the right visualize the data corresponding to the grouped time points per each feature assessed. Significance was tested via Student's t-test. 2-way ANOVA analysis was also performed and the significance is indicated in the bar-graph legends, N=3, n=8. **(e)** Manufacturer's OCR-graph, explaining the calculations underlying the relative respiratory capacity features. **(f)** Graphs showing the mitochondrial membrane potential (MMP) before the pooling in **Figure 3e**. Data was normalized to H1. Significance was tested via Student's t-test, N=4, n=2. For all panels, the data are presented as mean ± SEM. N indicates the number of experimental repetitions, n indicates the number of technical replicates per cell line.

Figure S3

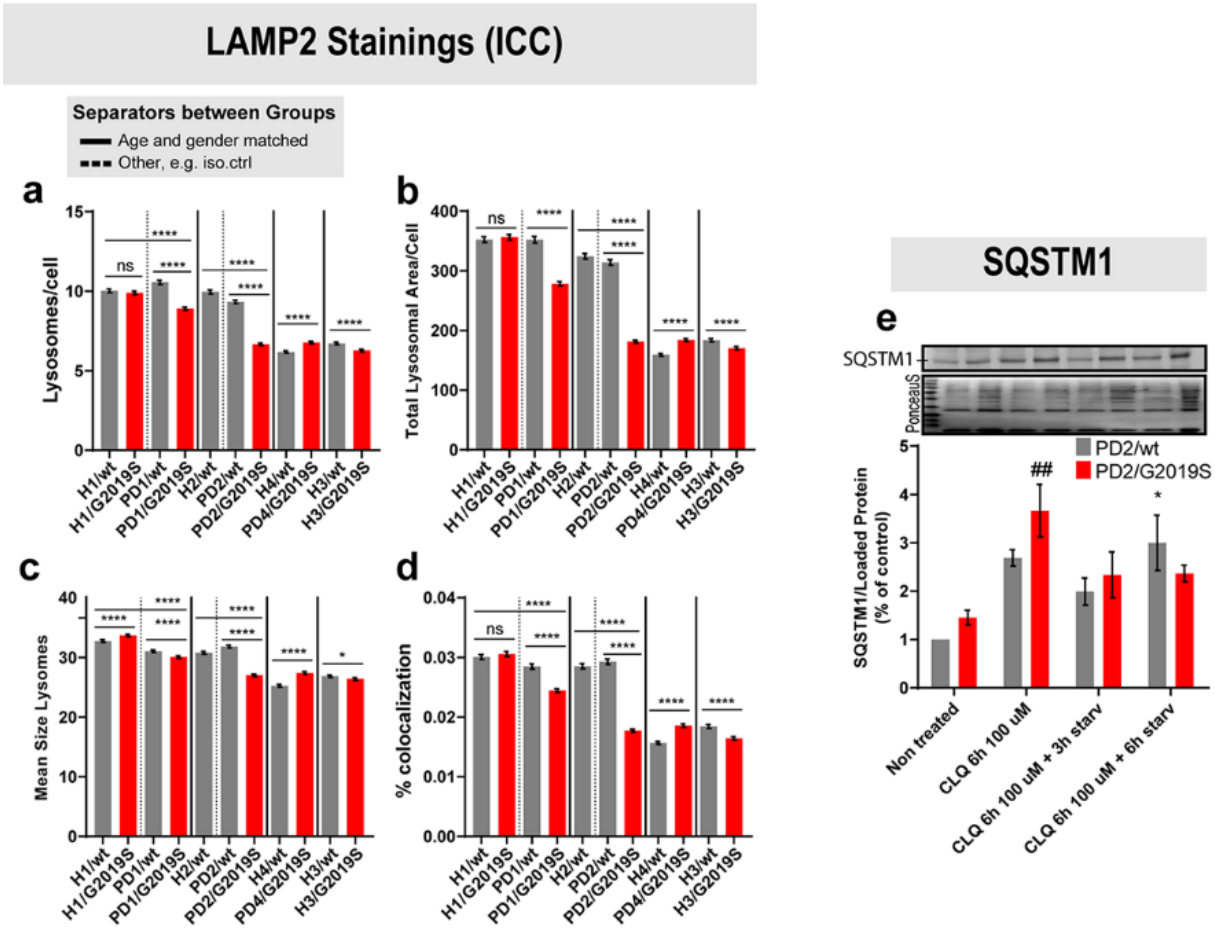

Figure S3. LRRK2-G2019S alters mitochondrial quality control in NESCs. Related to Figure 4.
(a-c) Bar graphs showing HCS analysis of the different cell groupings. **(a)** LAMP-2 puncta per cell, **(b)** total lysosomal area per cell, and **(c)** mean size lysosomes per cell (**Figures 4c-d**). Statistical significance was tested via Mann-Whitney test, N=3, n=3. **(d)** Graph showing the co-localization of LAMP-2 and TOM20 puncta per cell resulting from the HCS analysis, before the described pooling. Statistical significance was tested via Mann-Whitney test, N=3, n=3. **(e)** SQSTM1 level analysis shown for all conditions during the induction of autophagy via starvation, N=3, n=3. Statistical significance as determined by 2-way ANOVA and Tukey multiple comparisons test is indicated [* (comparison with untreated PD2.GC cells); ## (comparison with untreated PD2.G2019S cells)]. For all panels, the data are presented as mean ± SEM. N indicates the number of experimental repetitions, n indicates the number of technical replicates per cell line.

Table S1. Mitochondrial gene defined by the MitoCarta2.0.

Table S2. Differentially expressed genes identified when comparing LRRK2-WT and LRRK2-G2019S.

Supplemental Experimental Procedures

Cell Culture

iPSCs were maintained in E8 medium, on GelTrex matrix. Culture splits were performed using Accutase followed by overnight (o/n) incubation with 5 μM Y-27632 (Merck Millipore). NESCs were derived from iPSC as previously described (Reinhardt et al., 2013). Cells were maintained on MatriGel matrix NUNCLON plates. N2B27 maintenance media was used: Neurobasal, DMEM-F12 (1:1), 1x P/S, 1x L-Glutamine, B27 (1:100), N2 (1:200) (ThermoFisher) freshly supplemented with 3 μM CHIR(-99021) (Axon Medchem), 0.75 μM Purmorphamine (PMA) (Enzo Life Science) and 150 μM ascorbic acid (AA) (Sigma). Cells were seeded at $5*10^4$ cells/cm^2 (counted in a Countess II, AMQAX1000 ThermoFisher). For dopaminergic neuronal differentiation, NESCs were seeded at $5*10^4$ cells/cm^2 density either on MatriGel matrix coated NUNCLON or Cell Carrier-96 plates from Perkin Elmer for HCS analyses. Dopaminergic differentiation was initiated two days after initial cell seeding by the addition of differentiation media consisting of N2B27 freshly supplemented with: 10 ng/ml hBDNF (Peprotech), 10 ng/ml hGDNF (Peprotech), 500 μM dbcAMP (Peprotech), 200 μM ascorbic acid (Sigma), 1 ng/ml TGF-β3 (Peprotech), and 1 μM PMA (Enzo Life Science). PMA was withdrawn from the media after six days.

NGS preparation for Dropseq libraries

The 3' end enriched cDNA libraries were prepared by the tagmentation reaction of 600 pg cDNA library using the standard Nextera XT tagmentation kit (Illumina). The reactions were performed according to the manufacturer's instruction, except for the following two 400 nM primer sets (used instead of the kit provided primers): Primer 1 (AATGATACGGCGACCACCGAGATCTACACGCCTGTCCGCGGAAGCAGTGGTA TCAACGCAGAG T*A*C) and Primer 2 (N703: CAAGCAGAAGACGGCATACGAGATTTCTGC CTGTCTCGTGGGCTCGG for the PD2/G2019S samples and N709: CAAGCAGAAGACGGCATAC GAGATAGCGTAGCGTCTCGTGGGCTCGG for PD2/wt samples). The cycling program used for these samples was: 95°C for 30 s; fourteen cycles of 95°C for 10 s, 55°C for 30 s, 72°C for 30 s followed by a final extension step of 7°C for 5 min.Post PCR amplification, libraries were purified twice to reduce the primers and short DNA fragments, with 0.6x Agencourt AMPure XP beads (Beckman Coulter) followed by 1x Agencourt AMPure XP beads, in accordance with the manufacturer's protocol. Finally, the purified libraries were eluted in 15 μl of molecular grade water. Quality and quantity of tagmented cDNA library were evaluated using BioAnalyzer High Sensitivity DNA Chip. The average size of the tagmented libraries prior to sequencing was between 400-700.Purified Dropseq cDNA libraries were sequenced using an Illumina NextSeq 500 with the recommended sequencing protocol with the exception that 6 pM of custom primer (GCCTGTCCGCGGAAGCAGTGGTATCAACGCAGAGTAC) was used for priming of read 1. Further, paired-end sequencing was performed with reading 1 of 20 bases (covering the random cell barcode 1-12 bases and the rest 13-20 bases of the random molecular identifier, UMI) and read 2: 50 bases of the corresponding gene sequence.

Bioinformatics Processing of Dropseq data

FASTQ files were assembled from the raw BCL files using Illumina's bcl2fastq converter. FASTQ files were subsequently run through the FASTQC codes (Babraham bioinformatics; https://www.bioinformatics.babraham.ac.uk/projects/fastqc/) to check for the consistency in library qualities. The following parameters were evaluated for quality assessment: a) per base sequence quality (especially for read 2 of the gene related sequence); b) per base N content; c) per base sequence content and d) over-represented sequences. The libraries, which showed significant deviation, were re-sequenced. The FASTQ files were then merged and converted to binaries using PICARD's fastqtosam algorithm. Using the Dropseq bioinformatics pipeline, the sequencing reads were converted to digital gene expression matrix (DGE). The parameters used for the bioinformatics processing were consistent with the original Dropseq work (Macosko et al., 2015). To normalize the cells (equalize the transcript loading between the beads), the averaged normalized expression levels, $\log_2(TPM+1)$, was calculated. In accordance with the original Dropseq pipeline, to distinguish between the beads exposed to the cell and the beads which were blank, a cumulative function of the total number of transcripts per barcode was plotted. Then, a thresholding was performed on the resulting "knee plot" to estimate the beads exposed to the cell content. To filter the poor quality reads and cells reporting low transcript content, the following thresholds were used: only cells which expressed at least 1500 genes, and only genes expressed in at least 20 cells were considered for further analysis. The estimation of the highly variable genes and principal component analysis and tSNE dimensionality reduction was implemented

using SEURAT R package (http://satijalab.org/seurat/). The FASQT files have the GEO accession number GSE128040.

Analysis of Mitocondrial genes expression at the single cell level

Bioinformatics processing of the DropSeq data resulted in 8 gene expression matrices, one for each of the isogenic NESC pair (PD2/wt & PD2/G2019S) per time point extracted. Columns of these gene expression matrices represent individual cells, lines represent genes, and the entries represent the number of mRNA transcripts measured. The subsequent custom analysis pipeline was developed and implemented using Python programming language (version 3.6.0, with anaconda version 4.3.1). Since there was not a full overlap in genes of the resulting matrices, we first created for both genotypes at each time point a common list of expressed genes, which enabled us to analyze the pooled data of the NESC pair per time point. Moreover, in order to select only the highest quality data, we sorted the cells by the cumulative expression of all remaining genes. Only a subset of cells with the highest cumulative gene expression was considered for the analysis. In particular, only the 250 cells with the highest overall expression levels for each group (PD2/wt & PD2/G2019S) and each day were considered. The intention of this filtering step of all gene expression matrices was to attenuate the effect of noise originating from the acquisition process. It is worth mentioning that this conservative reduction to 2000 cells was more stringent than typical filtering in scRNA-seq quality control. Additionally, we normalized the gene expression matrix, for each particular group and day, by obtaining the standard score for each gene, i.e., we subtracted and divided the gene raw score of each cell respectively by the mean and the standard deviation of its row (gene).
To extract the relevant information on mitochondria, we defined a list of 1158 genes (**TABLE S1**) specific of mitochondria, based on MitoCarta2.0. We thus compared the expression of the corresponding genes between genotypes within sampling points. Since the gene expression levels are measured at the single cell level, instead of simply comparing the mean expression for all cells of each group, we analyzed the distribution of gene expression across cells. **Fig. 1c** histograms show the cumulative gene expression distributions for cells of each group and for each time point (columns). We defined cumulative gene expression as the sum of all mRNAs of the genes in the above mentioned list leading to a single cumulative score for each cell. Since the total numbers of mRNAs are not comparable between days, the values in the horizontal axis are normalized, separately for each day and each list of genes, to the maximum of the cumulative gene expression (across the genotypes PD2/wt & PD2/G2019S) for that particular time point. Thus, 1 corresponds to the maximal cumulative gene expression within one day, while 0 corresponds to no expression for each of the genes on the above mentioned list (**TABLE S1**), on that time point. Application of a z-test (corrected to allow the comparison of distributions with unequal variance) allowed assessing which individual panels present a statistically significant difference between the means of the cumulative gene expression of the genotypes. The test was corrected by including Bonferroni.

Analysis of differentially expressed genes (DEGs) in the single-cell RNA-Seq data

For each time point of the experiment, we determined how many genes were differentially expressed between LRRK2-WT and LRRK2-G2019S, by applying to all genes (independently for each gene) the following three statistical tests: a one-way ANOVA test, a one-way ANOVA test on ranks (Kruskal-Wallis test), and a test based on Mutual Information. The minimum p-value obtained by each gene across these three tests was retained, and any gene was considered differentially expressed with statistical significance when the corresponding p-value was below a threshold of 0.01.
In order to account for multiple testing, the Bonferroni correction was applied. The test was applied to all the approximately 20000 genes for each time point. The individual p-value for each gene is required to be $< 0.01/20000$ in order to claim statistical significance with an overall p-value < 0.01. We then computed the number of genes that were differentially expressed between genotypes with a statistical significance corresponding to a p-value < 0.01, for each day. In the results section, we also report the percentages, indicating how many of the mitochondrial specific genes are differentially expressed at each time point.

Immunocytochemistry

Cells were fixed using 4% paraformaldehyde (PFA) in 1x phosphosaline buffer (1xPBS), pH 7.4, for 15min at room temperature (RT). Unspecific antibody (AB) binding was avoided by blocking buffer incubation (5% FCS, 0.1%Tween20 in 1xTBST) for 1h at RT. Primary AB binding was performed for 48h at 4°C using indicated primary AB in blocking buffer. Three washing steps with 1xPBS were performed and the secondary ABs were incubated for

1h at RT (1:1000 dilution, including 1:1000 Hoechst33342). Following incubation, cells were washed 3x using 1xPBS. The following first antibodies were used: LAMP2 (DSHB, H4B4), and TOM20 (SantaCruz sc-11415).

2D Image analysis

Images were acquired sequentially on an Opera QEHS using a 60x (N.A. = 1.2) water immersion objective. Hoechst was excited at 405 nm laser and detected behind a 450/50 bandpass filter. Tom20_Alexa488 antibody was excited at 488 nm and detected behind a 520/35 bandpass filter. Lamp2_Alexa647 was excited at 640 nm and detected behind a 690/70 bandpass filter. Image analysis was implemented in Matlab (Mathworks). The Hoechst channel was low pass filtered, thresholded (>100), and connected components with less than 500 pixels were removed (NucleiMask1). Nuclei were split using a Laplacian of Gaussians of size 30 and standard deviation 10, thresholded (>0.12), and components with less than 2000 pixels were removed (NucleiContourMask). To refine the NucleiMask, the NucleiContourMask and resulting connected components with less than 2500 pixels were removed (NucleiMask2). Splitting was refined via Euclidean distance transform and watershed. Objects with less than 2500 pixels were removed (NucleiMask3). Cells were detected using low pass filtering of the phalloidin channel, thresholding (>20), and removal of connected components with less than 15000 pixels (CellMask). Single cell segmentation was based on Euclidean distance transform of NucleiMask3. Cells touching the image border were removed (CellStencil). For quality check, big objects (> 100000 pixels, NucleiMask4), as well as low sphericity objects were removed (NucleiMask5). The zones of the CellStencil passing this quality check were retained for further processing (CellStencilRefined). Mitochondria were segmented based on local image contrast as described previously (MitoMask), (Foster et al., 2016). Mitochondrial bodies were defined using image erosion of MitoMask with a sphere-shaped structuring element of radius 1. The mitochondrial surface was defined by subtracting the mitochondrial bodies from MitoMask (MitoSurfMask). Lysosomes were segmented based on the Lamp2 channel using a combination of local and global thresholding. For global thresholding, the raw channel was low pass filtered and thresholded (>75, LysoGlobalMask). For local thresholding, a difference of Gaussians was applied to the raw Lamp2 channel. The Foreground image was convolved with a Gaussian of size 10 and standard deviation 0.5 and the subtracted background image was convolved with a Gaussian of size 20 and standard deviation 5 (LysoDoG), and thresholded (>44, LysoLocalMask). The final lysosomal mask is the overlap between CellStencilRefined, LysoGlobalMask, and LysoLocalMask (LysoMask). Sphericity was computed according to Wadell. The feret ratio is the ratio between major and minor axis length. Colocalization is defined as the proportion of mitochondrial pixels overlapping with lysosomes.

Mitochondrial ROS measurement

Mitochondrial ROS analysis was performed in an adjusted protocol (Li et al., 2011). $2*10^5$ cells per sample were grown for two days reaching 70% confluence in 24 well plate. Cells were washed once using warm HBSS, incubated with 5µM MitoSOX in HBSS for 10 min at 37°C, and washed 3x using warm HBSS. Cells were detached using 0.05% trypsin for 5 min at 37°C. Trypsin was stopped using DMEM/F12+10%FCS. Cells were fixed using 4% PFA-PBS for 20 min at RT, washed with 1xPBS and suspended in 1%FBS/PBS. Cells were directly analyzed via flow cytometer. In FSC and SSC, we first gated the NESC population; next two gates were set on SSC-A vs. SSC-H and SSC-A vs. SSC-W to exclude doublets. Based on an unstained control a MitoSOX+ gate was set as indicated. Mean fluorescence of MitoSOX+ readout was plotted.

Extracellular flux (XF) analysis

NESC were seeded in MatriGel coated XF 96-well plates (Seahorse/Agilent) in octuplicates at $6.5*10^4$ cells/well in 100 µl growth medium. The Seahorse XF Cell Mito stress test kit was used according to manufacturer's instructions (Agilent). Oligomycin, FCCP, and Rotenone/Antimycin A were used at 1 µM concentration. After the assay, cells were frozen at -80 and CyQuant kit (ThermoFisher) was used to measure DNA content for normalization. The post-normalization values of OCR and ECAR reflect both the metabolic activities of the cells and the number of cells being measured. Data were further processed using the manufacturer's calculation matrix. Briefly, the determined parameters (basal respiration level, proton leak, maximal, spare, and non-mitochondrial respiratory capacity) were calculated according to manufacturer's instructions.

Propidium iodide

$2*10^5$ NESCs per sample were grown for four days, reaching 70% confluence. Cells were dissociated using Accutase incubation for 8 min, at 37°C. After 5 min 400 rcf centrifugation, cells were washed once in 1 ml ice cold DMEM/F12 w/o phenol-red. Cells were dissociated in 300 µl DMEM/F12 w/o phenol-red and stained with a final concentration of propidium iodide of 0.33 µg/ml for 2 min at 4°C. The samples were assessed using flow cytometry.

Total ROS measurement

NESCs were plated $1.5*10^4$ in 96-well plates and grown for 4 days in maintenance condition. GSH/GSSG-Glo Assay (Promega) was performed according to the manufacturer's instructions. White flat bottom plates (Corning) were used for final readout in a Tecan Infinity 200 pro plate reader.

Mitochondrial membrane potential and content measurement

$2*10^5$ NESCs per sample were grown for four days reaching around 70% confluence. Cells were dissociated using Accutase for 8 min, at 37°C. Cells were suspended in DMEM/F-12 w/o phenol red for imaging, washed once, and stained with different solutions. A) 5 nM TMRM medium; B) 5 nM TMRM + 0.1 µM MitoTracker Green FM (MTG); C) 5 nM TMRM + 5 µM FCCP. Cells were incubated for 30 min at 37°C. MTG samples were washed once using a stain-free medium. The resulting cell suspension was analyzed by a Fortessa flow cytometry analyzer (BD Biosciences). The analysis was performed using FlowJo. In FSC and SSC, we first gated the NESC population. The next two gates were set on SSC-A vs. SSC-H and SSC-A vs. SSC-W to exclude doublets. Due to the nonparametric distribution of some samples, median fluorescence values were extracted for TMRM and MTG staining. The TMRM median MMP representing intensities were normalized to MTG values representing mitochondrial content per cell. Median MTG Mitochondrial content values were used also separately for quantification of the mitochondrial content.

Western Blotting analysis

NESC were grown at $6.25*10^4$ for 1 week. 3 wells of of a six-well plate per condition were pooled for one sample. Cells were either not treated or incubated in: chloroquine 100µM for 6h in maintenance medium, 3h or 6h chloroquine 100 µM in EBSS for additional autophagy induction. Cells were washed once using ice-cold PBS, scraped off and pelleted. Cells were lysed with lysis buffer containing: 100 mM NaCl, 20 mM Tris (pH7.0), 2 mM EDTA, 2 mM EGTA ,and supplemented with 1% Triton X-100, 0.1% SDS, 1 mM PMSF, 1 mM DTT, 50 mM NaF, 1.5 mM sodium orthovanadate and 7x protease inhibitor cocktail (Roche). The lysates were sonicated twice during approximately 5 sec each (50% amplitude) and assayed for protein content using the BioRad reagent, according to the manufacturer's instructions and stored at -80°C. Equivalent amounts of protein (70 µg) were separated from SDS-PAGE gels and electroblotted onto polyvinylidene difluoride (PVDF) membrane in CAPS/methanol 10% at 0.75 A for 2 hours. The membranes were stained with a Ponceau-S solution and washed with distilled water and 0.1 M NaOH. Two further washes were carried out with TBS, 0.1% Tween (vol/vol), for 5 min each. The membranes were blocked with 5% bovine serum albumin (BSA) in TBS 0.1% Tween (vol/vol), for 60 min at RT and incubated o/n at 4ºC with agitation with antibodies against LC3B (Cell Signaling, 1:1000, 2775), SQSTM1/p62 (Cell Signaling, 1:1000, 5114), and Beclin-1 (BD Transduction Laboratories, 1:1000, 612113). The day after, the membranes were washed three times with 1% TBS-T containing BSA and further incubated with alkaline phosphatase-conjugated secondary antibody (1:10.000) for 1 hour at RT. Proteins were visualized by using an enhanced chemifluorescent reagent (ECF) and the bands were detected with the BioRad Chemidoc Imaging System. The detected bands were analyzed using Chemidoc Imaging System (BioRad) and normalized to intensity mean of PonceauS whole protein lane. We used PonceauS for normalization because we cannot exclude effects of LRRK2-G2019S on standard housekeeping proteins.

Supplemental Reference

Foster J, Koglsberger S, Trefois C, Boyd O, Baumuratov AS, Buck L, Balling R, Antony PM. Characterization of differentiated SH-SY5Y as neuronal screening model reveals increased oxidative vulnerability. **Journal of Biomolecular Screening**. 2016;21:469-509.

Li Z, Ji G, Neugebauer V. Mitochondrial reactive oxygen species are activated by mGluR5 through IP3 and activate ERK and PKA to increase excitability of amygdala neurons and pain behavior. **Journal of Neuorscience**. 2011;31:1114-1127.

Macosko EZ, Basu A, Satija R et al. Highly Parallel Genome-wide Expression Profiling of Individual Cells Using Nanoliter Droplets. **Cell**. 2015;161:1202-1214.

Reinhardt P, Glatza M, Hemmer K et al. Derivation and expansion using only small molecules of human neural progenitors for neurodegenerative disease modeling. **PloS One**. 2013:8e59252.